Journal of Colloid and Interface Science 708 (2026) 139861

Contents lists available at ScienceDirect

Journal of Colloid And Interface Science

journal homepage: www.elsevier.com/locate/jcis

Gold nanoparticles decorated with fluorinated poly(ethylene oxide): structural and functional insights

Matteo Cretella [a], Stefano Valente [a], Maria Şologan [a], Cristina Chirizzi [b,1], Francesca Baldelli Bombelli [b], Paolo Pengo [a], Paola Franchi [c], Marco Lucarini [c], Guilherme Carneiro Queiroz da Silva [d], Matteo Flaibani [d], Stefano Menichetti [e], Pierangelo Metrangolo [b], Paola Posocco [d], Lucia Pasquato [a,*]

[a] Department of Chemical and Pharmaceutical Sciences, University of Trieste, 34127 Trieste, Italy
[b] Laboratory of Supramolecular and Bio-Nanomaterials (SupraBioNanoLab), Department of Chemistry, Materials, and Chemical Engineering "Giulio Natta", Politecnico di Milano, 20131 Milan, Italy
[c] Department of Chemistry "G. Ciamician", University of Bologna, 40126 Bologna, Italy
[d] Department of Engineering and Architecture, University of Trieste, 34127 Trieste, Italy
[e] Department of Chemistry, University of Florence, 50019 Sesto Fiorentino, Florence, Italy

GRAPHICAL ABSTRACT

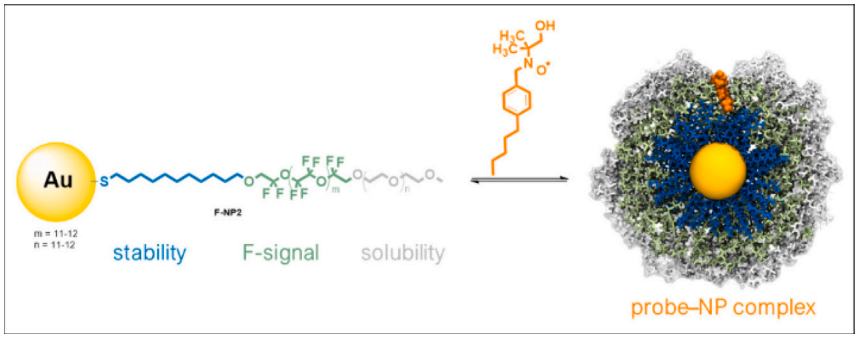

ARTICLE INFO

Keywords:
Fluorinated nanoparticles
Supramolecular chemistry
Self-assembled monolayers
Electron spin resonance
Hydrophobic binding
Molecular dynamics
^{19}F magnetic resonance imaging

ABSTRACT

Fluorinated hybrid organic–inorganic nanomaterials have attracted interest for applications ranging from biomedicine to superhydrophobic surfaces. However, few examples of fluorinated hybrid nanoparticles (F-NPs) establish a clear relationship between the structure of the fluorinated component and the properties of the hybrid system. This gap limits understanding of structure–property correlations and hinders the development of F-NPs with tailored functionalities. Here, we report the design, synthesis, and characterization of gold NPs passivated with fluorinated thiolates (**F-NP2**), combining high fluorine content with excellent dispersibility in both organic and aqueous solvents. The gold core measures approximately 2 nm, while the hydrodynamic diameter is around 12 nm, consistent with SAXS data. Electron Spin Resonance (ESR) studies reveal an exceptionally strong interaction between a hydrophobic radical probe and the NP coating, surpassing previously reported systems and

* Corresponding author.
E-mail address: lpasquato@units.it (L. Pasquato).
[1] Present address: Neuroradiology Unit, Fondazione IRCCS Istituto Neurologico Carlo Besta, 20133 Milano, Italy.

https://doi.org/10.1016/j.jcis.2026.139861
Received 4 November 2025; Received in revised form 18 December 2025; Accepted 8 January 2026
Available online 9 January 2026

indicating a high capacity for hosting hydrophobic, drug-like molecules. Molecular dynamics simulations support this behavior, showing a highly folded fluorinated segment and limited shielding by the polar mPEG550 end, which also explains reversible aggregation at high NP concentrations observed *via* dynamic light scattering. Finally, preliminary ^{19}F MRI data acquired at 7 T demonstrate a good signal-to-noise ratio, suggesting that these F-NPs may serve as sensitive fluorine-based tracking agents for biomedical applications.

1. Introduction

Hybrid organic-inorganic nanoparticles decorated with fluorinated ligands have attracted attention since the beginning of this century to obtain robust 3-D SAM [1,2], superhydrophobic surfaces [3–6], to achieve materials endowed with unexplored electronic properties [7], and as tracers for ^{19}F MRI [8–10]. Examples of silver and gold nanoparticles (Au NPs) coated with homoligand monolayers of perfluorinated alkyl and aryl thiolates have been shown to be dispersible in supercritical CO_2 and fluorinated solvents. [11–13] The introduction of fluorinated dodecanethiolates into the 3D self-assembled monolayer (SAM) of oleate ligands bound to the surface of PbS QDs has been shown to reduce the permeability of the ligand shell, due to their larger cross-sectional area compared to hydrogenated ligands, thus improving the passivation of the NP surface [7,14]. FePt NPs functionalized with varying degrees of fluorinated ligands were used to modulate surface properties, ranging from hydrophobic to superhydrophobic, when deposited as a thin film onto a surface [5]. Moreover, superhydrophobic surfaces could be obtained by casting a solution of fluorinated silica NPs over different substrates [2,15] and films of Au NPs protected by perfluorodecanethiolates exhibit an unexpected vapor response in which their conductivity increases upon exposure to analytes [16].

Au NPs coated by fluorinated alkanethiolate ligands (F-NPs) have also been explored in nanostructure imaging mass spectrometry (NIMS). Indeed, F-NPs promote a gentle laser desorption/ionization mechanism. This facilitates intact molecular ion formation with little background interference or molecular ion fragmentation to initiate the desorption/ionization mass spectrometry event while attenuating energy transfer to the analyte. This approach proved to be particularly useful for performing mass spectrometry-based metabolite imaging [17,18].

Limited dispersibility of these NPs in a variety of solvents has been observed for both linear and branched fluorinated ligands. This issue has been overtaken by their inclusion in nanoemulsions [9] or by decoration with suitable polymers [19]. Additional strategies to enhance the dispersibility of F-NPs include ligand modification *via* conjugation with short poly(ethylene oxide) end group [8,14], or glycosides [10] as well as the design of mixed monolayers, in which the fluorinated ligand is kept shorter and buried within the monolayer, while a longer co-ligand bearing a solvent-compatible end group is exposed at the surface, promoting solubility in the desired medium [20–23].

Besides ligands containing fluorinated alkyl or aryl moieties grafted on the inorganic surface of NPs, another emerging class of F-ligands contains fluorinated ethylene oxide units. Niikura and colleagues reported the synthesis of Au NPs passivated by thiolate ligands containing an alkyl chain close to the Au surface, followed by a semifluorinated four units ethylene oxide and an end group of two oxoethylene glycol units. The very short hydrophilic end group did not provide efficient shielding of the fluorinated moiety to the solvent and for this reason the NPs were found to form sub-100 nm Au NP vesicles (~60 nm in diameter) in tetrahydrofuran solution. The NPs vesicles were shown to be suitable for direct SERS detection of analytes in solution [24]. In order to stabilize the vesicular structure in water, a dithiol-PEG (MW 3400) was used as crosslinker together with a hydrophilic polymer. In such a way the hollow structure was dispersible in water and became a reservoir for drug storage and release triggered by short-term laser irradiation [25].

In the past, inspired by the work of Niikura, we designed thiol ligands consisting of a six- carbon alkyl chain adjacent to the Au surface, followed by a semifluorinated segment comprising four oxoethylene units and terminating with a methoxypolyethylene glycol 550 (mPEG550) to impart water dispersibility. Using these ligands we prepared ultrasmall Au NPs, **F-NP1**, Fig. 1, which proved to be highly robust, well dispersible in water, and suitable to be applied as tracer for ^{19}F MRI [8]. Moreover, these NPs demonstrated potential as very efficient drug carriers [26] and could be engineered to support both ^{1}H and ^{19}F MRI within the same NP [27]. However, a common issue with such systems, above mentioned, designed as tracers for ^{19}F MRI, is achieving both a high density of ^{19}F nuclei per NP and sufficient accumulation in the target tissue or cells to be properly detected.

To increase the number of quasi-equivalent F nuclei – and thus improve the signal-to-noise ratio (S/N) at the same NP concentration range - we conceived a thiol ligand following the same structural sequence as in **F-NP1**. Yet, in this case, we introduced a longer semi-fluorinated segment consisting of 12–13 fluorinated ethylene oxide units (F-PEO), based on the commercially available F-PEG600, and ending with mPEG550. The resulting nanoparticles, referred to as **F-NP2**, are shown in Fig. 1.

In our new ligand, the longer fluorinated polymer increases the number of quasi-equivalent F nuclei fivefold (from 8 in **F-NP1** to about 40 in **F-NP2**) potentially enhancing the S/N ratio at lower doses of F-NPs. A similar F-PEO unit has been conjugated to fluorescent dyes and successfully employed in nanoemulsions for ^{19}F MRI detection *in vitro* and *in vivo* in female BALB/c mice [28]. In this context, polymeric nanoparticles with high F-content in poly(perfluoropolyether) units have been reported to be excellent ^{19}F MRI tracers both *in vitro* and *in vivo* with high imaging sensitivity [29].

In addition, vesicular nanosystems formed through the co-assembly of proteins and fluoroamphiphiles prevent protein denaturation and facilitate membrane permeation in cells. Notably, increasing the fluorine content in fluoroamphiphiles enhances cellular uptake of the resulting vesicles, thereby improving the delivery of the proteins to the cytosol [30]. Longer fluorinated chains and higher degree of fluorination further improve payload delivery, up to a certain threshold. Indeed, beyond this point, excessive fluorophilicity causes the fluoroamphiphiles to segregate from the proteins, forming highly stable vesicles that fail to encapsulate and deliver the protein cargo.

Based on these elements, the choice of F-PEG600 as the fluorinated component represents a good compromise between a high number of fluorine atoms and a moderate level of fluorophilicity. Working with AuNPs offers several advantages. As prototypical hybrid organic-inorganic nanoparticles, they allow easier control over the degree of functionalization and the exposure/availability of functional groups compared to other nanosystems as soft nanoparticles. They can also be synthesized at ultrasmall sizes, which offer several advantages for biomedical applications, including enhanced tissue penetration, increased tumor accumulation *via* the enhanced permeability and retention (EPR) effect, improved biodistribution, facilitated cellular uptake, and potential renal clearance. Their high surface area further allows for easy functionalization, and their small size reduces the risk of blocking blood vessels and promotes a very labile protein corona [31].

Despite the promising ligand design, there were several elements that remained difficult to anticipate due to the lack of studies available on the fluorophilicity and conformation of F-PEO chains of this length in aqueous media and when confined within self-assembled monolayers (SAMs). Regarding the molecular conformation of the surface ligands, the chains may adopt a stretched, coiled, or intermediate configuration, depending on the so-called “brush regime” [32]. This regime is strongly

influenced by multiple factors, including, for instance, grafting chain density, Au core radius, and overall polymer chain length. Moreover, the three-layer architecture of the ligand introduces an additional level of complexity to its molecular structure and dynamic behavior in aqueous environment. Finally, the number of ligands per nanoparticle may change drastically depending on whether the polymeric chain adopts a linear or coiled conformation. In the latter case, our synthetic effort to increase the number of F atoms per nanoparticle may become ineffective. To address this, we reasoned that incorporating a longer spacer, compared to the one used in **F-NP1**, would ensure the formation of a well-packed SAM near the gold surface, while also supporting the grafting of the same number of ligands regardless of the conformation adopted by the F-PEO chains.

Here we report the synthesis of the **F-NP2**, along with an extensive characterization, which includes TEM, cryo-EM, TGA, DLS and SAXS measurements. Furthermore, we describe the ability of **F-NP2** to interact with hydrophobic probes *via* ESR experiments, we determine the ^{19}F T_1 and T_2 relaxation times and their performance as ^{19}F MRI tracer agent. Atomistic molecular dynamics (MD) calculations are also performed on both **F-NP1** and **F-NP2** to disclose the monolayer structure with molecular detail. **F-NP1** and **F-NP2** binding behavior, including the interaction with a hydrophobic radical probe, is also evaluated using MD simulations and compared with the ESR outcomes. Such a comprehensive investigation allows for the rational tuning of F-NP properties, including dispersibility in organic or aqueous media, self-assembly, the ability to sequester small molecules, and their use as drug carriers and imaging tracers.

2. Experimental

2.1. Synthesis

Detailed procedures for the preparation of the fluorinated thiol and its characterization are described in Supplementary Material (SM). **F-NP2** were synthesized through a homogeneous phase reaction following previous works [8,33]. The thiol ligand (236.54 mg, 0.108 mmol) was dissolved in a round bottom flask in deoxygenated methanol (50 mL) under an argon atmosphere. In a 20 mL vial, tetrachloroauric acid trihydrate (64 mg, 0.163 mmol) was dissolved in Milli-Q water under argon atmosphere and transferred in a three neck round bottom flask. The methanol solution of the ligand was transferred to the three-neck flask by a positive argon pressure *via* a cannula and the mixture was stirred for 30 min at RT, cooled at 0 °C and kept at this temperature for 30 min. A freshly prepared solution of 0.1 M $NaBH_4$ (67.63 mg, 1.79 mmol) in 17.9 mL of Milli-Q water was then added dropwise to the reaction mixture in 3.5 min. The colour of the solution turned to dark violet; the mixture was stirred at 0 °C for one hour and then at RT for 2 h. After this period, the solvent was partially removed in vacuum and the F-NPs solution was transferred in a 15 mL Falcon tube. To this mixture, 3 mL of hexane was added, and the F-NPs were centrifuged (4000 rpm, 10 min, RT). The supernatant was discarded, and the procedure was repeated three more times. The F-NP were then dispersed in MilliQ water and dialysed against MilliQ water for two days at RT while changing the water every day. TEM: d = 2.1 ± 0.8 nm. UV–Vis (methanol): λ_{max} = 503 nm (broad). DLS (Milli-Q water): d_H = 11.55–12.71 nm. TGA: organic loss = 78%, t = 350 °C. ^1H NMR (400 MHz, acetone-d_6) δ: 4.15–3.95 (br, mPEG-OCH_2CF_2 + Au@S-$(CH_2)_{11}$-OCH_2CF_2), 3.80–3.45 (br, mPEG, −[O-CH_2-CH_2], 3.30 (s, OCH_3) 1.85–1.00 (br, aliphatic H). ^{19}F NMR (376 MHz, acetone-d_6) δ: = −78 -79.69 (br, Au-$(CH_2)_{11}$-OCH_2CF_2- + − CF_2-CH_2OmPEG), −87.50-90.30 (m), −90.69 (m, −[O-CF_2-CF_2]$_n$-). T_1 relaxation time (400 MHz, D_2O, Inversion recovery pulse sequence): T_1 (25 °C) = 474 ms, T_1 (37 °C) = 434 ms. T_2 relaxation time (400 MHz, D_2O, CPMG pulse sequence): T_2 (25 °C) = 23 ms, T_2 (37 °C) = 25 ms.

3. Results and discussion

3.1. Synthesis and characterization of F-NP2

The synthesis of the fluorinated ligand was inspired by the Ahrens paper in which the commercially available symmetric F-PEO dicarboxylic methyl ester, upon functionalization, was used in nanoemulsion for ^{19}F-MRI and fluorescence detection [28]. This led us to consider the use of an amide linkage to conjugate the PEG550 moiety to one end of the F-

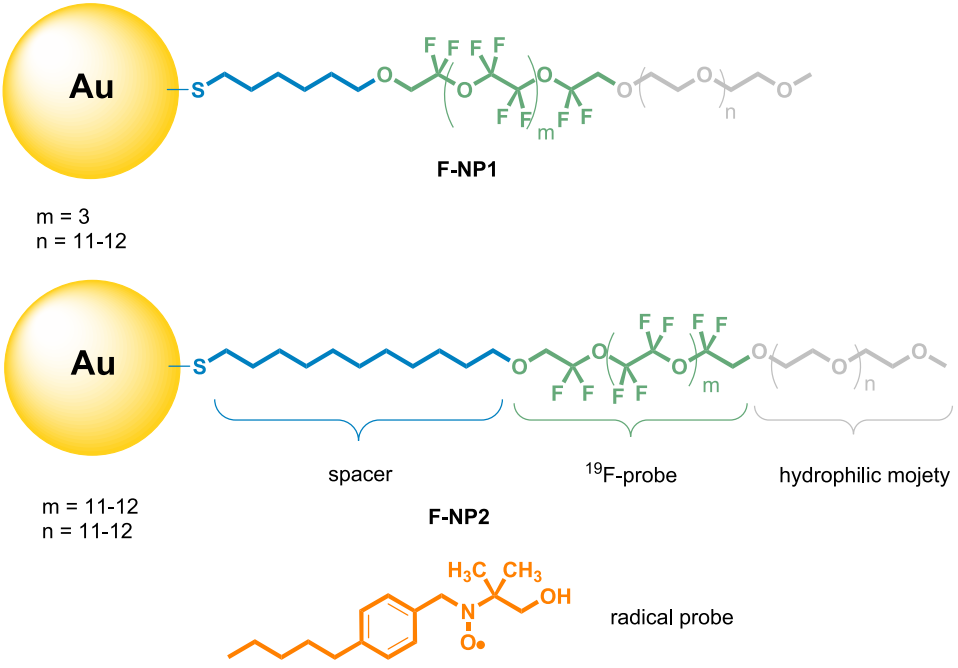

Fig. 1. Schematic representation of the previously reported gold **F-NP1** [8] and the newly developed **F-NP2**, featuring an eleven-carbon alkyl spacer and the fluorinated polymer F-PEO, along with the chemical structures of the ligands and the radical probe employed in ESR and MD studies. (For interpretation of the references to colour in this figure legend, the reader is referred to the web version of this article.)

polymer, and an alkyl chain bearing a thiol group to the other end, thereby enabling grafting onto the gold surface of the NP. However, this strategy was not successful for several reasons: i) the esters groups of fluorinated carboxylic acids are activated and the corresponding amides hydrolyse more easily than classical amides because of the electron-withdrawing effect of the fluorinated chain. In our hands, the F-PEG ester and amide proved to be too labile for the synthetic steps necessary to prepare the desired ligand. ii) Because of the strong reactivity of the F-PEO derivatives, purification steps are challenging and iii) the desymmetrization product of the commercial F-PEO ester could be obtained with low chemical yield. For these reasons, we switched to the F-PEO alcohol, which could be efficiently modified through the Williamson ether synthesis (see Scheme S1). The detailed synthesis of the F-ligand and its characterization are reported in the SM.

The synthesis of the **F-NP2** followed a previous preparation protocol developed by our group and it is described in Section 2 [26,27]. Nanoparticles are characterized by a core diameter of 2.1 ± 0.81 nm and 98 thiolates, based on TEM and TGA, respectively, Fig. 2, in line with the number of ligands expected with hydrogenated ligands, likely thanks to the presence of the long alkyl spacer [34]. Consistently, the average composition for **F-NP2** is $Au_{310}Ligands_{98}$ [34]. Inspection of cryo-EM images displays an average diameter of 6.8–7.0 nm, Fig. 2 D, in agreement with the diameter of the gold core plus the fluorinated layer obtained by computational studies reported in section 2.5.

DLS measurements of **F-NP2** in water were carried out at different NPs concentrations ranging from 250 μg/mL to 16 μg/mL in water. At all concentrations, aggregates are detected, as indicated by the intensity distribution graphs. However, the aggregation appears to be reversible: upon dilution, the proportion of species with a hydrodynamic diameter (d_H) above 100 nm decreases significantly, favoring the formation of nanosystems with a d_H of approximately 12 nm. This trend is supported by the number distribution graphs and the increase in count rate (kcps) observed upon dilution, as shown in Figs. 3 and S20.

3.2. SAXS measurements

SAXS experiments were performed on **F-NP2** samples at different concentrations (0.1, 1.0, 5.0, 10.0 mg/mL) for obtaining information on the local structure of the NPs (Fig. 4A). The samples were measured at RT and 37 °C (see Fig. S21 in SM) and showed the same scattering pattern indicating no change in structure with temperature. The curves normalized to NP concentration differ significantly in the low-q region showing an increase in scattering intensity with concentration, while the intermediate-low q region was similar for all samples, except at 0.1 mg/mL (see inset Fig. 4A). We interpreted this behavior as due to the agglomeration observed by DLS, which might be more accentuated for higher concentrations. Based on TEM results indicating a core size of 2.1 nm, we first analyzed the SAXS curves using a polydisperse spherical particle form factor with a core–shell structure assuming the starting scattering length density (SLD) of the core to be equal to that of pure gold, and that of the shell as an intermediate value among the various organic components (see details on the fitting analysis in SM). Of note, partitioning the shell into distinct compartments with diverse SLD did not significantly improve the fitting. The results were satisfactory only for the two lowest concentrations with a good fit for $q \geq 0.015$ Å^{-1}, while at lower q values the fitting curve began to deviate from the experimental data (see Fig. 4 B red dashed line and Table 1), likely due to the observed agglomeration. The results indicate the presence of NPs with a core of 2.4 nm and an organic shell of 3.6 nm yielding an overall size of 9.6 nm, which is in good agreement with the number-weighted DLS size distribution, see Table 1. To consider the agglomeration factor, we decided to analyze the SAXS curves with a fractal model. This model reproduces the scattering from a fractal structure with a primary building block of polydisperse core-shell spheres (see SM, page 18). The primary building blocks were first modeled using the obtained structural parameters from the polydisperse core-shell fitting analysis of the samples at low concentration. This fitting analysis worked well in the entire q-range only for the lowest two concentrations indicating the formation of agglomerates of about 50 nm, while it did not reproduce the high-q

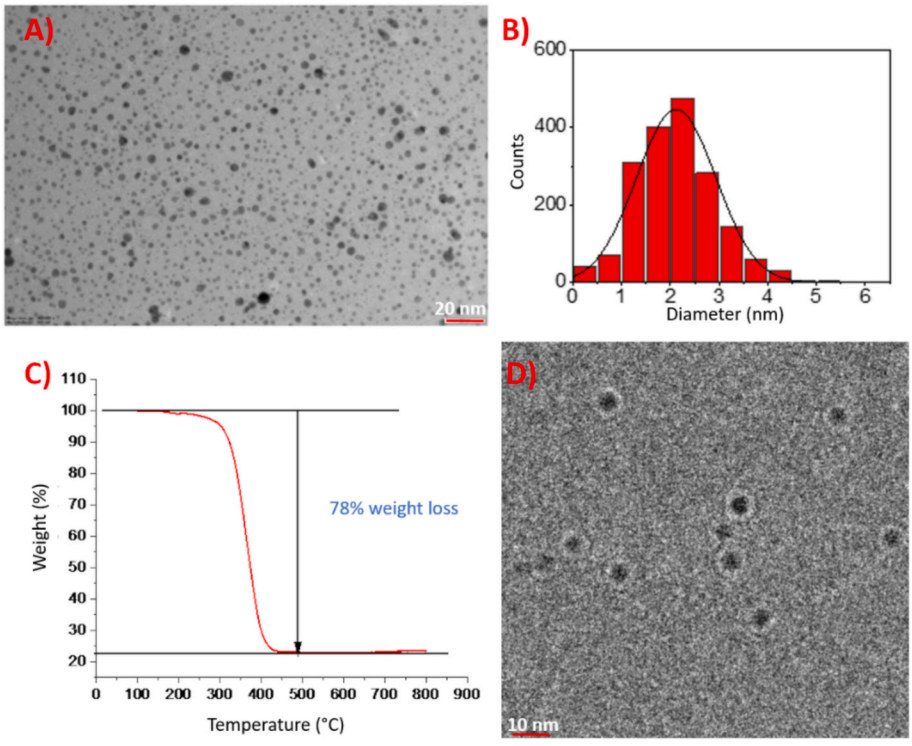

Fig. 2. A) Representative TEM image of **F-NP2**, scale bar 20 nm, and B) dimensional analysis; C) TGA and D) representative cryo-EM image, scale bar 10 nm, of **F-NP2**.

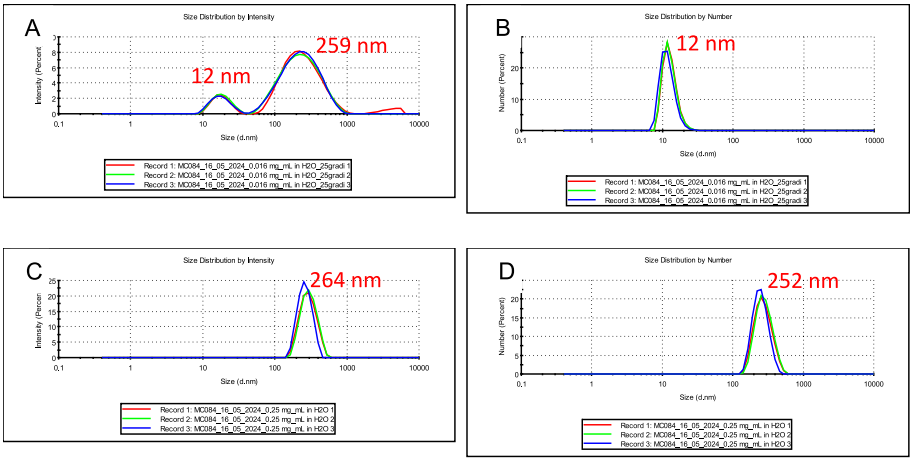

Fig. 3. DLS measurements of **F-NP2** at different concentrations in water: A) and B) 16 μg/mL by Intensity and Number respectively, C) and D) at 250 μg/mL by Intensity and Number, respectively.

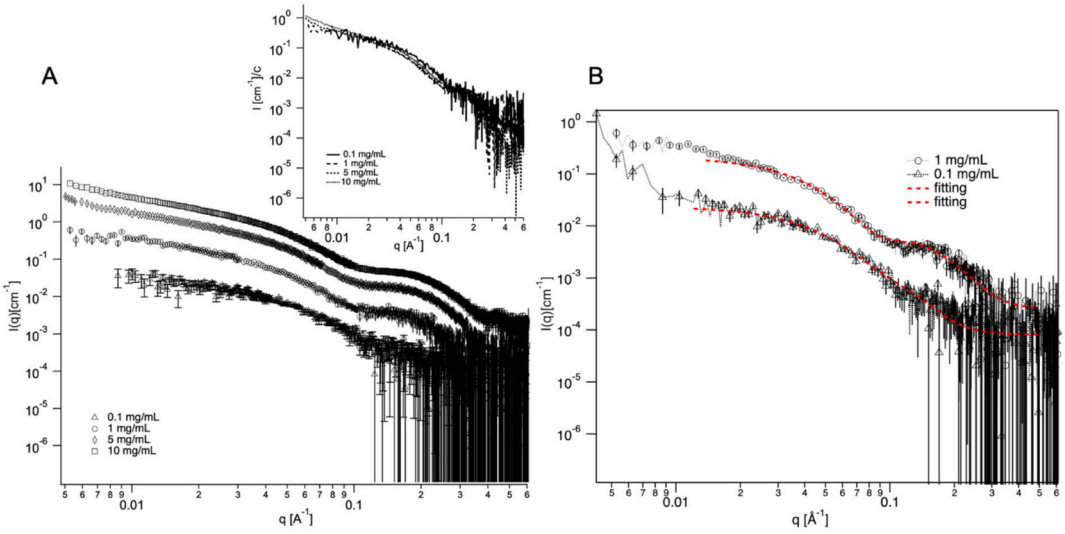

Fig. 4. (A) SAXS curves of **F-NP2** at 0.1 mg/mL (triangles), 1 mg/mL (circles), 5 mg/mL (rhombus) and 10 mg/mL (square) measured at RT. The inset shows the same curves normalized for the NP concentration. (B) SAXS curves of **F-NP2** at 0.1 mg/mL (triangles) and 1 mg/mL (circles) measured at RT and analyzed with a polydisperse spherical particle form factor with a core-shell structure (red dashed line). (For interpretation of the references to colour in this figure legend, the reader is referred to the web version of this article.)

Table 1
Fitting parameters of the SAXS analysis reported in Fig. 4.

Volume fraction (f)	R_{core} (Å)	R_{shell} (Å)	Polydispersity	SLD core ($Å^{-2}$)	SLD shell ($Å^{-2}$)
6×10^{-6}	12	36.05 ± 0.43	0.3	1.32e-04 ± 1.1e-06	1.43e-05 ± 6.05e-08
6×10^{-5}	12	36.05 ± 0.43	0.3	1.04e-04 ± 5.6e-07	1.38e-05 ± 2.8e-08

region of the two curves at higher concentrations indicating a more complex agglomeration pattern for these samples (see Fig. S22 and Table 1 in SM).

3.3. ^{19}F MRI

The ^{19}F NMR spectrum of **F-NP2** is characterized by two intense broad signals at −90.21 and − 90.69 ppm attributed to the perfluorinated oxoethylene units, and two signals at −79.03 and − 79.40 ppm corresponding to the CF_2 linked to the alkyl chain on one side and to the PEG550 moiety on the other (Fig. S16). T_1 and T_2 of **F-NP2** in D_2O, measured on the most intense signal, at 9 T are 434 ms and 25 ms respectively. These results suggest that these NPs have suitable relaxometric properties for ^{19}F MRI allowing to use fast-imaging methods, as shown by the optimal ^{19}F MRI response of the phantoms of **F-NP2** dispersions at different concentrations reported in Fig. 5, for which the signal resulted above the detection limit for concentration ≥ 5 mg/mL.

3.4. ESR investigation

In recent years, we have utilized CW-ESR spectroscopy and spin probes to investigate the properties of 3D-SAM [8,14,20,22,26,35]. In this study, we applied this technique using *para-n*-pentyl benzyl hydroxyalkyl nitroxide (Fig. 1) as the radical probe. Fig. 6 presents the ESR spectrum of the nitroxide, which was generated directly inside an ESR tube by oxidizing the corresponding amines (1 mM) with Oxone (1 mM) in the presence of **F-NP2** at 338 K in water.

The resulting spectrum displays two distinct sets of signals, corresponding to the radical existing in equilibrium between the monolayer phase and the free nitroxide. As generally observed, both nitrogen (a_N)

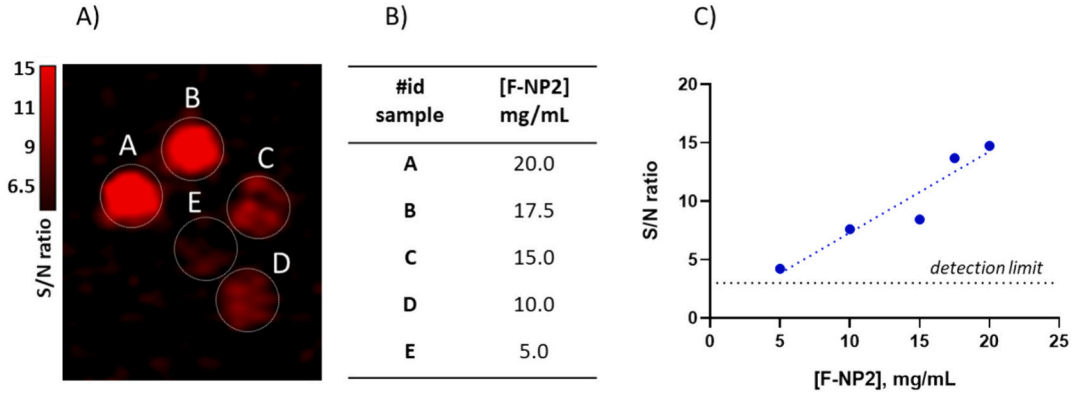

Fig. 5. (A) Representative ^{19}F MRI image of samples containing different concentrations of **F-NP2**, labeled A to E. (B) Table summarizing the **F-NP2** concentration (mg/mL) for each sample. (C) Plot of S/N ratio as a function of **F-NP2** concentration, showing a linear trend and detectable signal even at the lowest concentration (5 mg/mL).

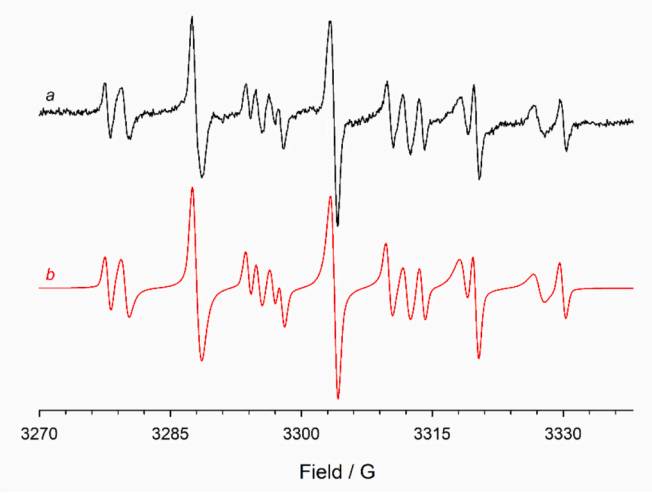

Fig. 6. ESR spectrum of the radical probe recorded in the presence of **F-NP2** (1.6×10^{-3} M of ligands) at 338 K. In red is reported the corresponding theoretical simulation obtained by employing the spectroscopic parameters reported in Table 2. (For interpretation of the references to colour in this figure legend, the reader is referred to the web version of this article.)

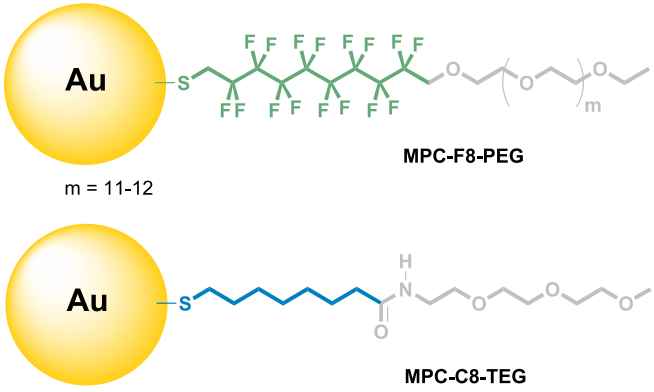

Fig. 7. Schematic representation of the previously reported Au NPs: **MPC-F8-PEG** [14] and **MPC-C8-TEG** [35].

and benzylic protons (a_{2H}) coupling constants significantly decrease when the aminoxyl is situated in the less polar monolayer environment. This leads to notable differences in the resonance fields for the $m_I(2H) \pm 1$ lines of the two spectra. A similar reduction in coupling constants was previously observed in our studies on other protected Au NPs [20], which was attributed to the increased stabilization of nitroxide mesomeric forms in low-polarity media, where the unpaired electron is more localized on the oxygen atom rather than nitrogen.

Further comparison of the a_N and a_{2H} values for radicals within **F-NP2**, **F-NP1** [8], and other related nanoparticles such as **MPC-F8-PEG** [14] and **MPC-C8-TEG** [35] monolayers (Fig. 7) reveals that these parameters are notably lower in the former (see Table 2). Based on these data, different hypothesis can be put forward: i) the probe may be more deeply embedded within the monolayer of **F-NP2**, making it less exposed to the water molecules; ii) alternatively, the probe may engage in a greater number of fluorine-based interactions due to the longer F-PEO chains, which are energetically more favorable compared to interactions with hydrogenated carbon chains [36]. However, with increasing temperature, the a_N value increases significantly, indicating a possible reorganization of the monolayer that promotes the exposure of the probe to a more polar environment.

We calculated the equilibrium constant (K_{eq}) for the partitioning of the probe between water and the fluorinated monolayer measuring the ratio of the probe concentration in the monolayer to that of the free species for a given concentration of **F-NP2**. The probe ratio was determined by theoretical simulation of ESR spectra (see Fig. 6). The equilibrium constant derived from this study at 298 K (K_{eq} = 4438 M^{-1}) is significantly higher than that previously estimated at the same temperature for monolayer protected NPs with a similar three-layer structure but a shorter fluorinated moiety (**F-NP1**) and similar core size (K_{eq} = 593 M^{-1}). The increase is even larger when comparing these results with **MPC-F8-PEG** with an averaged core size of 2.5 nm (K_{eq} = 176 M^{-1}) or **MPC-C8-TEG** with an averaged core size of 1.4 nm (K_{eq} = 104 M^{-1}). The K_{eq} is the ratio between the rate constant of formation of the complex probe-monolayer and the rate constant of disruption of the complex. Following this line of reasoning, we may argue that the fluorinated amphiphiles adopt a structure that promotes the formation of lipophobic pockets, encountered by the radical probe, enabling highly energetic

Table 2
Spectroscopic parameters for the radical probe in different monolayers and partition equilibrium (K_{eq}) constants.

NP	T (K)	a_N (G)	a_{2H} (G)	K_{eq} (M^{-1})	Ref.
F-NP2	298	14.65	8.52	4438	This work
F-NP2	318	15.04	8.45	3475	This work
F-NP2	338	15.21	8.45	2512	This work
F-NP1	298	15.45	8.65	593	8
MPC-F8-PEG	298	15.46	8.68	176	14
MPC-C8-TEG	298	15.67	8.97	104	35

interactions that are responsible for a much slower release of the probe from the monolayer compared to the rate constants observed in the other fluorinated monolayers studied. This clearly suggests that the investigated monolayer can solubilize small hydrophobic molecules far more effectively than the NPs studied in our previous works.

3.5. MD calculations

Atomistic MD simulations were carried out on **F-NP1** and **F-NP2** to reveal the molecular structure of the SAM and its organization in water. As shown in Fig. 8A and C, ligands in **F-NP1** adopt a globular conformation around the gold core, with the PEG550 segment placed on the outer part of the monolayer. This arrangement suggests a stratified shell, where the F-PEO chain is shielded by the PEG550 terminal layer to minimize interactions between water molecules and the fluorinated polymer. Radial Distribution Function (RDF) analysis of the ligand and its individual segments (Fig. 8E) supports this hypothesis, revealing a layered organization: the alkyl spacer is the closest to the core, followed by the F-PEO segment, and then the PEG550 component, which directly interfaces with the solvent. Different considerations can be made for **F-NP2** (Fig. 8B and D). The longer alkyl spacer and the higher number of fluorinated units lead to a broadening of the inner hydrophobic region (Fig. 8F). This effect is further enhanced by the stretching and bundling of the alkyl ligand portion (Fig. 8D), which promotes the fanning out of the chains. Notably, the F-PEO tends to coil back on itself, seeking interactions with the inner, less hydrated region of the monolayer. The time-averaged end-to-end distance of F-PEO in **F-NP2** is 15.0 Å (± 3.6), corresponding to a ~ 70% reduction compared to its fully extended length (49.4 Å). A similar, though less pronounced, trend was observed in **F-NP1**, with a 40% chain folding.

The PEG550 segments lie flat over the F-PEO shell. In **F-NP2**, the F-PEO layer is partially exposed, making it more accessible to the surrounding environment than in **F-NP1**. This effect likely arises from the larger dimensions of **F-NP2**, both in terms of the gold core and the molecular weight of the F-PEO. Given that the PEG component is identical in both systems, it appears insufficient to fully cover the surface

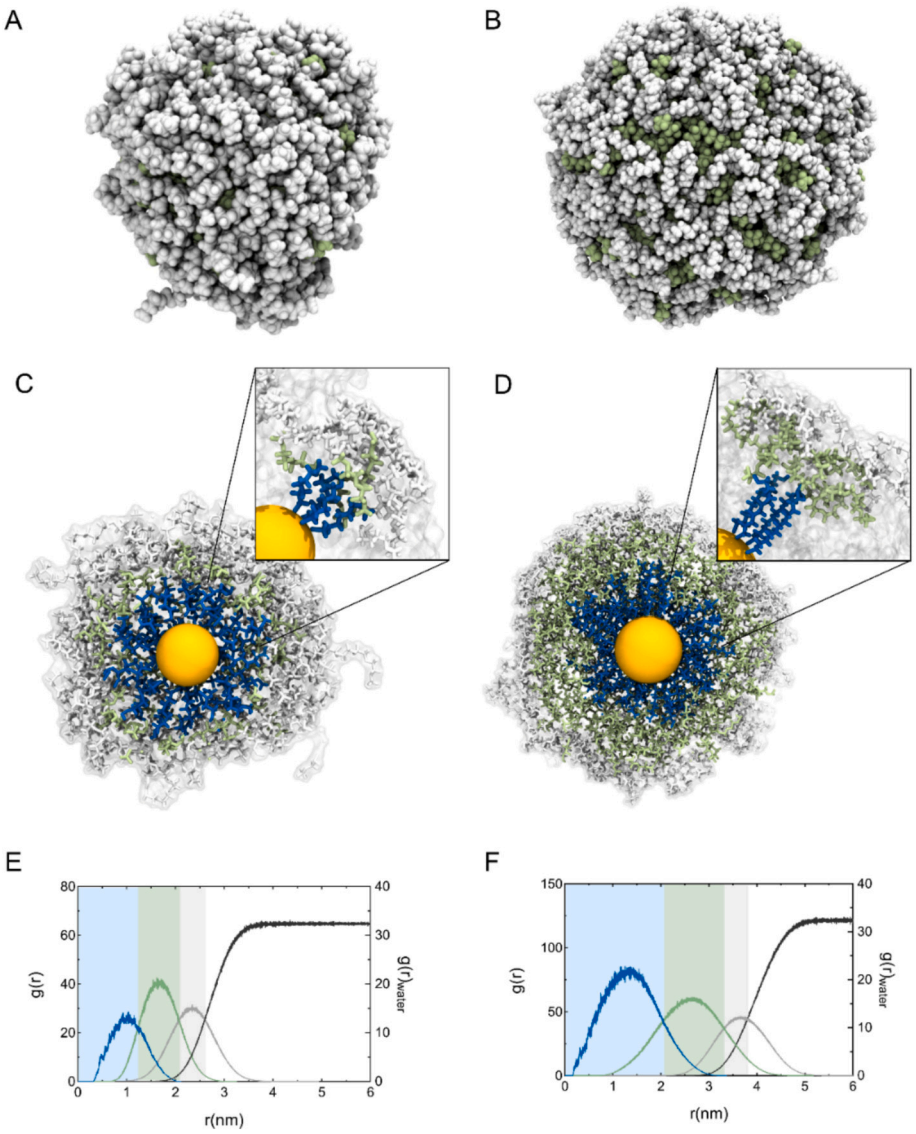

Fig. 8. Molecular structure and cross-section of **F-NP1** (A and C) and **F-NP2** (B and D), obtained from MD calculations accounting for explicit water molecules (omitted here for clarity). Cross-section views illustrate the layered organization of the monolayer, with the insets highlighting ligand conformations of selected neighboring chains. Colour legend: alkyl spacer, blue; F-PEO, green; PEG, white; gold, yellow. Radial distribution functions g(r) for solvent and ligands of **F-NP1** (F) and **F-NP2** (G). The g(r) for the different ligand chain segments follows the same colour scheme as in the molecular structure. The g(r) of water is reported in black (right axis). (For interpretation of the references to colour in this figure legend, the reader is referred to the web version of this article.)

in **F-NP2**, as it does in **F-NP1**. The lower grafting density observed in **F-NP2** further limits surface coverage. The RDF analysis of the entire ligand allowed for an estimation of the overall monolayer thickness in **F-NP2** (3.8 nm), which closely aligns with the value obtained from SAXS measurements.

Next, the interaction with the radical probe employed in the ESR studies was investigated. Unbiased MD calculations supported the spontaneous binding of the probe to both monolayers. Fig. 9A visually compares the probe interaction site in **F-NP1** and **F-NP2**. In addition to that, a set of descriptors was monitored over the simulation time, trying to capture some relevant molecular features of the environment surrounding the probe. These include: the solvent-accessible surface area (SASA) of the probe, which measures its accessibility upon binding; the number of probe contacts with the F-PEO segment; the PEG550 ligand portion; and the alkyl spacer, the number of water molecules in direct contact with the probe (Fig. 9B).

Despite the high mobility of the probe within each monolayer, the environments it encounters appear to be different in **F-NP1** and **F-NP2**. The key distinction lies in the number of F atoms shaping the binding site, which is higher in **F-NP2** than in **F-NP1**. Moreover, in **F-NP1**, the probe interacts more with PEG550. Differences in SASA and surrounding water are less pronounced, aligning with the molecular structures showing that the incomplete shielding of the fluorinated layer in **F-NP2** allows water accessibility and leaves the probe solvent exposed. Therefore, the increased hydrophobicity sensed by the ESR probe, and reflected in the low a_N for **F-NP2**, is likely to be attributed to the enhancement of the interactions between the probe molecule and nearby fluorinated methylene groups. Thus, the energy associated with the interactions between the probe and the F-PEO section of the monolayer may be responsible for the 7.5 times larger K_{eq} measured in **F-NP2** with respect to **F-NP1**.

4. Conclusions

We have introduced a highly robust and water-dispersible F-NP (**F-NP2**) passivated with ligands containing a F-PEO segment composed of 12–13 fluorinated oxoethylene units, terminating with a mPEG chain of comparable length. TEM, cryo-EM, SAXS and DLS analysis reveal a gold core diameter of 2.1–2.4 nm and an organic shell thickness of approximately 4 nm. This suggests that the F-PEO adopts a folded structure and, due also to the curvature of the NP surface, the mPEG chains are insufficient to fully cover the fluorinated region as evidenced by the presence of reversible aggregates at high NPs concentrations in DLS measurements. The exposure of fluorinated zones may enhance the interaction of the **F-NP2** with cell membranes as reported in the Introduction [30]. MD simulations reveal the formation of bundles among the alkyl chains spacers, as well as the tendency of the F-PEO component to lie on the alkyl portion of the monolayer, avoiding extension into the solvent and instead adopting a tangled conformation. Similarly, the ending mPEG appears to spread over the surface of F-PEO to mask it as much as possible from the solvent, while still leaving some fluorinated regions exposed to water. As a consequence, the surface morphology of **F-NP2** is rather different from that of a similar system bearing a shorter F-PEO part (**F-NP1**). This also impacts their interaction with small molecules, as demonstrated by ESR studies. Indeed, the ability of **F-NP2** to bind a hydrophobic probe, with a K_{eq} of 4438 M^{-1} at 25 °C, is approximately 7.5 times greater than that measured for **F-NP1**. This is well above the fivefold increase in the number of fluorine atoms – which enhances the number of possible interactions of the probe with F atoms – suggesting that the effect is more likely due to the structural features of the monolayer and the interaction energy between fluorine atoms and the radical probe, as supported by the MD simulations [36].

Preliminary ^{19}F MRI data, acquired at 7 T with non-optimized acquisition parameters, show a good signal-to-noise (S/N) ratio at a concentration of 4.8 × 10^{18} fluorine atoms/mL, which could be further improved by reducing the size of the gold core and using innovative MRI pulse sequences [37].

In conclusion, **F-NP2** has proven to be particularly promising due to its unique structure and its ability to undergo reversible aggregation–disaggregation processes. Its high capacity to entrap hydrophobic molecules provides a strong foundation for future developments in the biomedical field, as well as for applications in the sequestration of hydrophobic pollutants—both currently under investigation by our group.

CRediT authorship contribution statement

Matteo Cretella: Writing – original draft, Investigation, Formal analysis, Data curation. **Stefano Valente:** Methodology, Investigation, Formal analysis, Data curation. **Maria Şologan:** Methodology, Investigation, Formal analysis, Data curation. **Cristina Chirizzi:** Writing – original draft, Methodology, Investigation, Formal analysis, Data curation. **Francesca Baldelli Bombelli:** Writing – review & editing, Writing – original draft, Supervision, Methodology, Investigation, Formal analysis, Data curation. **Paolo Pengo:** Methodology, Investigation, Formal analysis. **Paola Franchi:** Writing – review & editing, Writing – original draft, Methodology, Investigation, Formal analysis, Data curation. **Marco Lucarini:** Writing – review & editing, Writing – original draft, Supervision, Methodology, Investigation, Formal analysis, Data curation, Conceptualization. **Guilherme Carneiro Queiroz da Silva:** Methodology, Investigation, Formal analysis, Data curation. **Matteo Flaibani:** Methodology, Investigation, Formal analysis, Data curation. **Stefano Menichetti:** Writing – original draft, Methodology, Investigation, Formal analysis, Data curation. **Pierangelo Metrangolo:** Supervision, Resources, Funding acquisition. **Paola Posocco:** Writing – review & editing, Writing – original draft, Supervision, Methodology, Investigation, Formal analysis, Data curation. **Lucia Pasquato:** Writing – review & editing, Writing – original draft, Supervision, Funding acquisition, Formal analysis, Data curation, Conceptualization.

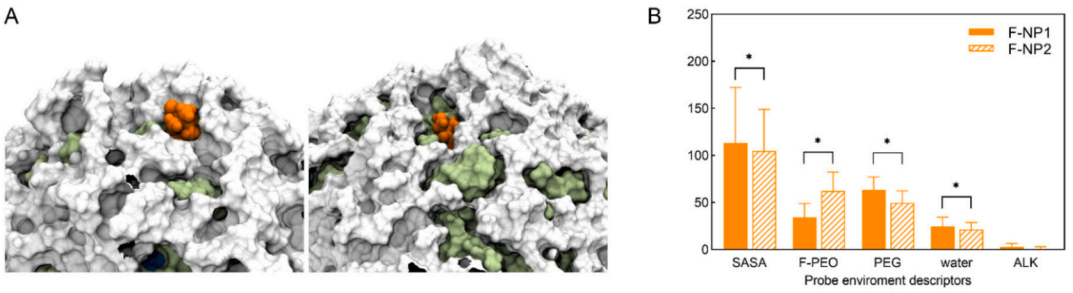

Fig. 9. A) Location of the ESR probe (orange) interacting with the monolayer in **F-NP1** (left) and **F-NP2** (right). PEG550 and F-PEO components are represented as white and green surfaces, respectively. B) Molecular features of the environment surrounding the ESR probe. From left to right: solvent-accessible surface area (*SASA*, $Å^2$); number of heavy atoms from the fluorinated polymer (*F-PEO*); number of heavy atoms from the PEG550 segment (*PEG*); number of nearby water molecules (*water*); and number of heavy atoms from the alkyl spacer (*ALK*). Atoms within 6 Å of the heavy atoms of the probe were considered in contact. * $p < 0.01$, *t*-test. (For interpretation of the references to colour in this figure legend, the reader is referred to the web version of this article.)

Declaration of competing interest

The authors declare the following financial interests/personal relationships which may be considered as potential competing interests: Reports a relationship with that includes:. Has patent pending to. If there are other authors, they declare that they have no known competing financial interests or personal relationships that could have appeared to influence the work reported in this paper.

Acknowledgements

This research was supported by the Italian Ministry of Research through the project "NiFTy" PRIN 2017 grant no. 2017MYBTXC and the University of Trieste. GCQDS, MF and PP are grateful to CINECA under the ISCRA initiative for high-performance computing resources. The authors thank Dr. Annalisa Guerri for the technical support in Cryo-TEM measurements performed in the FloCEN Florence Center for Electron Nanoscopy of the University of Florence. Small Angle X-rays Scattering (SAXS) measurements were performed at the Next-GAME Laboratory of the Politecnico di Milano, co-funded by Regione Lombardia. The authors thank the Experimental Imaging Center at IRCCS Ospedale San Raffaele (Milan, IT) for facilitating access to the preclinical MRI scanner.

Appendix A. Supplementary data

Synthesis and characterization of the fluorinated ligand; Characterization of **F-NP2**; Fitting analysis of the SAXS curves; Computational methods. Supplementary data to this article can be found online at [https://doi.org/10.1016/j.jcis.2026.139861].

Data availability

Data will be made available on request.

References

[1] D.J. Weinberg, C. He, E.A. Weiss, J. Am. Chem. Soc. 138 (2016) 2319–2326.
[2] H.J. Lee, A.C. Jamison, T.R. Lee, J. Phys. Chem. C 122 (2018) 13911–13919.
[3] Y. Ofir, B. Samanta, P. Arumugam, V.M. Rotello, Adv. Mater. 19 (2007) 4075–4079.
[4] H. Zhou, H. Wang, H. Niu, A. Gestos, X. Wang, T. Lin, Adv. Mater. 24 (2012) 2409–2412.
[5] H. Wang, J. Fang, T. Cheng, J. Ding, L. Qu, L. Dai, X. Wang, T. Lin, Chem. Commun. (2008) 877–879.
[6] C. Pereira, C. Alves, A. Monteiro, C. Magén, A.M. Pereira, A. Ibarra, M.R. Ibarra, P. B. Tavares, J.P. Araújo, G. Blanco, J.M. Pintado, A.P. Carvalho, J. Pires, M.F. R. Pereira, C. Freire, ACS Appl. Mater. Interfaces 3 (2011) 2289–2299.
[7] A. Dass, R. Guo, J.B. Tracy, R. Balasubramanian, A.D. Douglas, R.W. Murray, Langmuir 24 (2008) 310–315.
[8] M. Boccalon, P. Franchi, M. Lucarini, J.J. Delgado, F. Sousa, F. Stellacci, I. Zucca, A. Scotti, R. Spreafico, P. Pengo, L. Pasquato, Chem. Commun. 49 (2013) 8794–8796.
[9] V. Dichiarante, I. Tirotta, L. Catalano, G. Terraneo, G. Raffaini, M.R. Chierotti, R. Gobetto, F. Baldelli Bombelli, P. Metrangolo, Chem. Commun. 53 (2017) 621–624.
[10] O. Michelena, D. Padro, C. Carrillo-Carrión, P. del Pino, J. Blanco, B. Arnaiz, W. J. Paraka, M. Carril, Chem. Commun. 53 (2017) 2447–2450.
[11] P.S. Shah, J.D. Holmes, R.C. Doty, K.P. Johnston, B.A. Korgel, J. Am. Chem. Soc. 122 (2000) 4245–4246.
[12] T. Yonezawa, S. Onoue, N. Kimizuka, Langmuir 17 (2001) 2291–2293.
[13] N.M. Sangeetha, S. Bhat, G. Raffy, C. Belin, A. Loppinet-Serani, C. Aymonier, P. Terech, U. Maitra, J.-P. Desvergne, A. Del Guerzo, Chem. Mater. 21 (2009) 3424–3432.
[14] C. Gentilini, F. Evangelista, P. Rudolf, P. Franchi, M. Lucarini, L. Pasquato, J. Am. Chem. Soc. 130 (2008) 15678–15682.
[15] X.-Y. Wang, C. Zhang, S. Sun, M. Kalulu, L. Chen, X. Zhou, Y. Jiang, Coll. Surf. A 578 (2019) 123550.
[16] J. Im, A. Chandekar, J.E. Whitten, Langmuir 25 (2009) 4288–4292.
[17] M.E. Kurczy, Z.-J. Zhu, J. Ivanisevic, A.M. Schuyler, K. Lalwani, A.F. Santidrian, J. M. David, A. Giddabasappa, A.J. Roberts, H.J. Olivos, et al., Nat. Commun. 6 (2015) 5998.
[18] A. Palermo, E.M. Forsberg, B. Warth, A.E. Aisporna, E. Billings, E. Kuang, H. P. Benton, D. Berry, G. Siuzdak, ACS Nano 12 (2018) 6938–6948.
[19] M. Carril, D. Padro, P. del Pino, C. Carrillo-Carrión, M. Gallego, W.J. Parak, Nat. Commun. 8 (2017) 1542.
[20] C. Gentilini, P. Franchi, E. Mileo, S. Polizzi, M. Lucarini, L. Pasquato, Angew. Chem. Int. Ed. 47 (2009) 3060–3064.
[21] S. Bidoggia, F. Milocco, S. Polizzi, P. Canton, A. Saccani, B. Sanavio, S. Krol, F. Stellacci, P. Pengo, L. Pasquato, Bioconjug. Chem. 28 (2017) 43–52.
[22] C. Gabellini, M. Şologan, E. Pellizzoni, D. Marson, M. Daka, P. Franchi, L. Bignardi, S. Franchi, Z. Posel, A. Baraldi, P. Pengo, M. Lucarini, L. Pasquato, P. Posocco, ACS Nano 16 (2022) 20902–20914.
[23] J.M. Arango, D. Padro, J. Blanco, S. Lopez-Fernandez, P. Castellnou, P. Villa-Valverde, J. Ruiz-Cabello, A. Martin, M. Carril, ACS Appl. Mater. Interfaces 13 (2021) 12941–12949.
[24] K. Niikura, N. Iyo, T. Higuchi, T. Nishio, H. Jinnai, N. Fujitani, K. Ijiro, J. Am. Chem. Soc. 134 (2012) 7632–7635.
[25] K. Niikura, N. Iyo, Y. Matsuo, H. Mitomo, K. Ijiro, ACS Appl. Mater. Interfaces 5 (2013) 3900–3907.
[26] M. Boccalon, S. Bidoggia, F. Romano, L. Gualandi, P. Franchi, M. Lucarini, P. Pengo, L. Pasquato, J. Mater. Chem. B 3 (2015) 432–439.
[27] M. Şologan, F. Padelli, I. Giachetti, D. Aquino, M. Boccalon, G. Adami, P. Pengo, L. Pasquato, Nanomaterials 9 (2019) 879.
[28] J.M. Janjic, M. Srinivas, D.K.K. Kadayakkara, E.T. Ahrens, J. Am. Chem. Soc. 130 (2008) 2832–2841.
[29] C. Zhang, S.S. Moonshi, W. Wang, H.T. Ta, Y. Han, F.Y. Han, H. Peng, P. Král, B. E. Rolfe, J.J. Gooding, K. Gaus, ACS Nano 12 (2018) 9162.
[30] Z. Zhang, W. Shen, J. Ling, Y. Yan, J. Hu, Y. Cheng, Nat. Commun. 9 (2018) 1377.
[31] M. Epple, V.M. Rotello, K. Dawson, Acc. Chem. Res. 56 (2023) 3369–3378.
[32] J.C. Conrad, M.L. Robertson, J. Am. Chem. Soc. Au 3 (2023) 333–343.
[33] P. Pengo, S. Polizzi, M. Battagliarin, L. Pasquato, P. Scrimin, J. Mater. Chem. 13 (2003) 2471–2478.
[34] M.J. Hostetler, J.E. Wingate, C.-J. Zhong, J.E. Harris, R.W. Vachet, M.R. Clark, J. D. Londono, S.J. Green, J.J. Stokes, G.D. Wignall, G.L. Glish, M.D. Porter, N. D. Evans, R.W. Murray, Langmuir 14 (1998) 17–30.
[35] M. Lucarini, P. Franchi, G.F. Pedulli, P. Pengo, P. Scrimin, L. Pasquato, J. Am. Chem. Soc. 126 (2004) 9326–9329.
[36] D. Marson, F. Guida, M. Şologan, S. Boccardo, P. Pengo, F. Perissinotto, V. Iacuzzi, E. Pelizzoni, S. Polizzi, L. Casalis, L. Pasquato, S. Pacor, A. Tossi, P. Posocco, Small 15 (2019) 1900323.
[37] R.B. van Heeswijk, W.R. Bauer, F. Bönner, J.M. Janjic, W.J.M. Mulder, L. M. Schreiber, J. Schwitter, U. Flögel, Adv. Cardiovascular Imaging 16 (2023) e014742.